Recovery Timescales of the Dayside Martian Magnetosphere to IMF Variability

N. Romanelli, G. Dibraccio, Ronan Modolo, François Leblanc, J. Espley, J. Gruesbeck, J. Halekas, J. Mcfadden, B. Jakosky

Geophysical Research Letters

RESEARCH LETTER
10.1029/2019GL084151

Recovery Timescales of the Dayside Martian Magnetosphere to IMF Variability

N. Romanelli[1,2], G. DiBraccio[1], R. Modolo[3], F. Leblanc[3], J. Espley[1], J. Gruesbeck[1], J. Halekas[4], J. Mcfadden[5], and B. Jakosky[6]

[1]Solar System Exploration Division, NASA Goddard Space Flight Center, Greenbelt, MD, USA, [2]CRESST II, University of Maryland, Baltimore County, Baltimore, MD, USA, [3]Laboratoire Atmosphere, Milieux et Observations Spatiales (LATMOS), IPSL, CNRS, UVSQ, UPMC, Paris, France, [4]Department of Physics and Astronomy, University of Iowa, Iowa City, IA, USA, [5]Space Sciences Laboratory, University of California, Berkeley, CA, USA, [6]Laboratory for Atmospheric and Space Physics, University of Colorado Boulder, Boulder, CO, USA

Key Points:
- Hybrid numerical simulation results are used to estimate recovery timescales of the dayside Martian magnetosphere to IMF variability
- Recovery timescales of the dayside magnetosphere range between 8 s and 11 min for a 50-s IMF rotation, depending on the considered region
- O^+ plume recovery timescales increase in the downstream direction (up to $1R_M$ from the terminator) and are close to the sheath O^+ gyroperiod

Correspondence to:
N. Romanelli,
norberto.romanelli@nasa.gov

Citation:
Romanelli, N., DiBraccio, G., Modolo, R., Leblanc, F., Espley, J., Gruesbeck, J., et al. (2019). Recovery timescales of the dayside Martian magnetosphere to IMF variability. *Geophysical Research Letters*, *46*, 10,977–10,986. https://doi.org/10.1029/2019GL084151

Received 18 JUN 2019
Accepted 9 SEP 2019
Accepted article online 12 SEP 2019

Abstract In this work we revisit an event observed by Mars Atmosphere and Volatile Evolution MissioN in the solar wind where the interplanetary magnetic field (IMF) rotates around the Mars-Sun axis during ~6 min. Based on a time-dependent LATMOS Hybrid Simulation, we determine recovery timescales of the dayside Martian magnetosphere normalized by the IMF variability timescale. Particularly, we find that such recovery timescales range between 8 s and 11 min for an ~90° IMF rotation that lasted 50 s (observed as part of the 6-min time interval), depending on the considered magnetospheric region. We also find that the O^+ plume recovery timescales range between 40 and 120 s, taking greater values for further downstream distances (at least up to $1R_M$ downstream from the terminator plane). This range is on the order of the magnetosheath O^+ gyroperiod, showing the kinetic nature of the plume recovery process.

1. Introduction

The Martian magnetosphere forms as the solar wind (SW) directly interacts with the planet's upper atmosphere and crustal magnetic fields. This interaction constantly changes based on both planetary (e.g., crustal field orientation and ionosphere conductivity) and solar factors (e.g., SW parameters and extreme ultraviolet flux). Additionally, various acceleration mechanisms directly affect the spatial and temporal scales of the system (e.g., Brain et al., 2017; Curry et al., 2015; Dubinin et al., 2011; Harada et al., 2015a; 2015b; Halekas et al., 2017, 2017; Jakosky et al., 2018; Ma et al., 2017; Martinez et al., 2019; Mazelle et al., 2004; Modolo et al., 2012; Rahmati et al., 2017; Romanelli, Modolo, Leblanc, Chaufray, Hess, et al., 2018; Sánchez-Cano et al., 2017). Indeed, acceleration by Hall electric fields, magnetic reconnection, and plasma instabilities associated with non-Maxwellian distribution functions are examples of physical processes that depend upon several variables and that affect the evolution of the plasma in the Martian environment on different spatial and temporal scales. Given the wide range of processes acting on the magnetosphere, it is challenging to quantify the impact that changes in one of the external/internal conditions might have on the overall SW interaction with Mars.

One key external factor affecting the responses of the Martian-induced magnetosphere (Acuña et al., 1998) to the upcoming SW is the interplanetary magnetic field (IMF) variability. Such variability affects the evolution of planetary pickup ions (Dong et al., 2015), the magnetotail morphology (e.g., DiBraccio et al., 2015; DiBraccio et al., 2017; DiBraccio et al., 2018; Dubinin & Fraenz, 2015; Fang et al., 2018; Grigorenko et al., 2017; Hurley et al., 2018; Luhmann et al., 2015; Romanelli et al., 2014; Romanelli et al., 2015), and magnetic reconnection (Harada et al., 2015a, 2015b) with Martian crustal magnetic fields (Acuña et al., 1999; Connerney et al., 2001, 2005), among other processes. In order to characterize transient magnetospheric states and estimate recovery timescales associated with changes in the IMF orientation, we analyze a case study under restricted external conditions. This case study utilizes a combination of single-point in situ spacecraft observations by the Mars Atmosphere and Volatile EvolutioN (MAVEN) mission (Jakosky et al., 2015) along with time-dependent hybrid simulations (Modolo et al., 2012; Romanelli, Modolo, Leblanc, Chaufray, Hess, et al., 2018).

Specifically, in this work we further analyze the simulation results presented by Romanelli, Modolo, Leblanc, Chaufray, Hess, et al. (2018) when MAVEN observed an IMF rotation in the upstream SW on 23

December 2014, between 10:43 and 10:49 UT. Romanelli, Modolo, Leblanc, Chaufray, Hess, et al. (2018) reported that recovery timescales in the Martian magnetotail range between ∼10 s and ∼12 min and that the computed H^+ and O^+ planetary ion loss rates do not show a strong change due to such IMF rotation. However, the recovery timescales of the dayside Martian magnetosphere and the spatiotemporal adaptation of O^+ plume to this event remain an open question. Here, we build from this original work to examine the MAVEN data and Romanelli, Modolo, Leblanc, Chaufray, Hess, et al. (2018) simulation in order to determine the recovery timescales of the dayside Martian magnetosphere and the O^+ plume.

This study is structured as follows. We provide a brief description of MAVEN Magnetometer (MAG; Connerney, Espley, Lawton, et al., 2015), Solar Wind Ion Analyzer (SWIA; Halekas et al., 2015), and the LatHyS code in section 2. Recovery timescales of the Martian dayside magnetosphere and the O^+ plume are computed in section 3. We present our discussion and conclusions in section 4.

2. Data and Model Overview

The MAVEN MAG provides vector magnetic field measurements with a maximum sampling frequency of 32 Hz and absolute vector accuracy of 0.05% (Connerney, Espley, Lawton, et al., 2015; Connerney, Espley, DiBraccio, et al., 2015). In this study we have used full time resolution MAG data, only in the finest dynamic range, corresponding to an accuracy of ∼0.25 nT.

MAVEN's SWIA is an energy and angular ion spectrometer covering an energy range between 25 eV/q and 25 keV/q with a field of view of 360° × 90° (Halekas et al., 2015). In this work we display the observed energy ion flux spectra with 8-s resolution. Moments derived from SWIA (Halekas et al., 2015) and Supra-Thermal and Thermal Ion Composition (STATIC; McFadden et al., 2015) measurements (not shown) were used as input for the time-dependent simulation (Romanelli, Modolo, Leblanc, Chaufray, Hess, et al., 2018).

LatHyS is a global three-dimensional multispecies parallelized hybrid model that is able to accurately describe physical processes occurring in space plasma environments (e.g., Leclercq et al., 2016; Modolo et al., 2005; Modolo et al., 2012; Modolo, 2016; Modolo et al., 2017; Richer et al., 2012; Romanelli, Modolo, Leblanc, Chaufray, Hess, et al., 2018; Romanelli, Modolo, Leblanc, Chaufray, Martinez, et al., 2018; Turc et al., 2015). To model the Martian environment, it considers six ion species kinetically: SW H^+_{SW} and He^{++}_{SW} and planetary H^+, O^+, O_2^+, and CO_2^+. The electrons are described with two massless fluids with different temperatures (SW and ionospheric). The Martian neutral environment is modeled by one-dimensional radial density profiles for CO_2, O, and H, assuming spherical symmetry. Profiles used in this study correspond to RUN B, reported in Modolo (2016). Crustal magnetic fields at Mars (Acuña et al., 1999) are described using the model derived in Cain et al. (2003). A detailed description of the LatHyS model and the time-dependent simulation presented here can be found in Modolo (2016) and Romanelli, Modolo, Leblanc, Chaufray, Hess, et al. (2018), respectively.

The time-dependent simulation analyzed in this work has 80-km spatial resolution and 0.0617-s time step (i.e., 0.0333 Ω_{ci}^{-1}, where Ω_{ci} is the SW protons gyrofrequency). The simulation domain extends from −2.4 to 2.4 R_M in X_{MSO} axis and from −4.5 to 4.5 R_M in Y_{MSO} and Z_{MSO} axes (R_M stands for Martian radii, 1 R_M=3,393 km). The Mars Solar Orbital (MSO) coordinate system is centered at Mars and is defined as follows: The X_{MSO} axis points to the center of the Sun, and the Y_{MSO} axis points opposite to the direction of the orbital velocity component of Mars orthogonal to X_{MSO}. The Z_{MSO} completes the right-handed system.

3. Analysis and Results

Building on the work of Romanelli, Modolo, Leblanc, Chaufray, Hess, et al. (2018), we analyze an event on 23 December 2014, between 06:00 and 14:15 UT, when MAVEN observed an IMF rotation in the upstream SW. An overview of MAVEN SWIA and MAG observations, along with MAVEN's 4.5-hr orbit trajectory in MSO coordinates, is displayed in Figure 1. The inbound bow shock crossings occurred at the flank (close to the terminator plane), and the outbound crossings were closer to the bow shock subsolar point. As reported in Romanelli, Modolo, Leblanc, Chaufray, Hess, et al. (2018), MAVEN observations suggest that the mean IMF, mean bulk SW velocity, and mean SW density remained approximately constant when the spacecraft was inside the magnetosphere during the first orbit (07:17–09:20 UT). Specifically, these parameters did not vary significantly when comparing upstream, inbound and outbound, observations. The computed mean

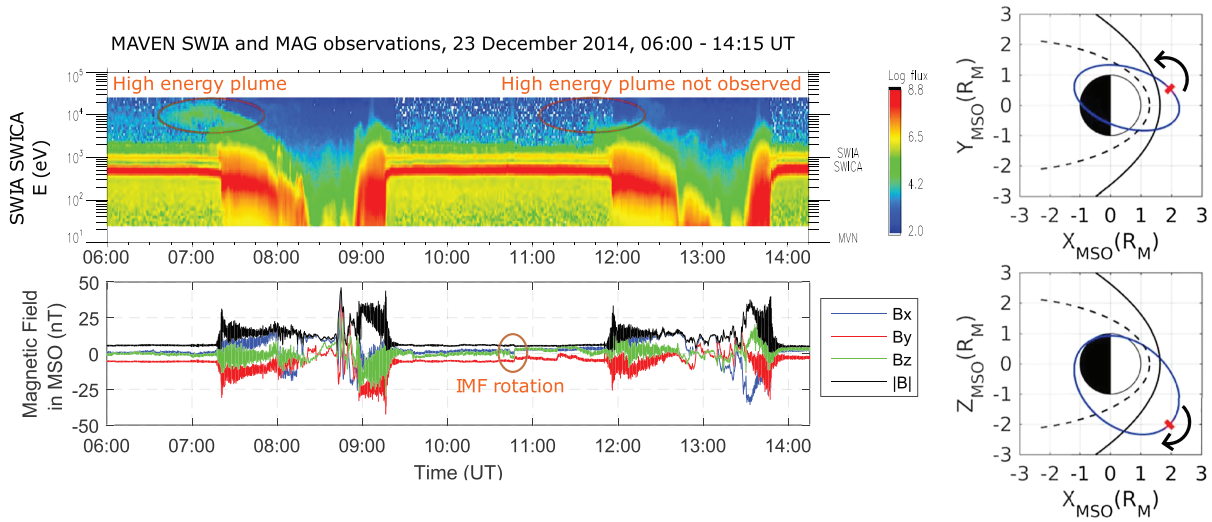

Figure 1. (left panels) MAVEN MAG and SWIA (SWICA mode) observations on 23 December 2014, 06:00–14:15 UT. The SWIA ion flux energy spectrogram (top) and the magnetic field MSO components and magnitude as a function of time (bottom). (right panels) MAVEN trajectory in MSO coordinates for this time interval (shown in blue). Red points display MAVEN's position when the IMF rotation analyzed in this work takes place. Bow shock and magnetic pileup boundary fits (Vignes et al., 2000) are shown in solid and dashed black lines, respectively. MAVEN = Mars Atmosphere and Volatile Evolution MissioN; MAG = magnetometer; SWIA = Solar Wind Ion Analyzer; MSO = Mars Solar Orbital; IMF = Interplanetary Magnetic Field.

IMF, SW velocity, and density (in MSO coordinates) are $\mathbf{B_{IMF}}$=[0.59±0.56,−5.41±0.27,−1.16±0.65] nT, $\mathbf{U_{SW}}$=[−298±3,29±3,24±6] km/s, and n_{SW}=11±0.5 cm^{-3}, respectively. These estimations correspond to the average of the mean value of each variable derived from inbound (06:45–07:15 UT) and outbound (09:36–10:06 UT) measurements. Variability in the IMF orientation was first observed between 10:43 and 10:49 UT where, in particular, a ∼90° rotation in the clock angle occurred over ∼50 s centered around 10:47 UT. Upstream SW velocity and density did not vary significantly during this time interval.

3.1. Dayside Magnetosphere Recovery Timescales

LatHyS results are employed to determine recovery timescales of the dayside magnetosphere to the observed IMF rotation on 23 December 2014 (Figures 2a and 2b). We use four slices at various X_{MSO} distances in the Y_{MSO}-Z_{MSO} planes in order to analyze the local magnetic field morphology throughout the dayside magnetosphere and the near wake: X_{MSO}=1.25R_M, X_{MSO}=1R_M, X_{MSO}=0R_M, and X_{MSO}=−1R_M. The first plane is chosen to intersect the magnetic pileup boundary (MPB) close to its subsolar point based on the analytical model presented by Vignes et al. (2000). The other three slices are chosen to determine changes in the magnetic field morphology on 1-R_M length scales, centered at the terminator plane. Note that the spatial region under analysis is complementary to the one considered by Romanelli, Modolo, Leblanc, Chaufray, Hess, et al. (2018) to compute magnetotail recovery timescales.

For each of these planes, we consider four annular regions centered on Y_{MSO}=Z_{MSO}=0R_M defined by the following (cylindrical) radial limits: r=[r_{SPH},r_1], r=[r_1,r_{MPB}], r=[r_{MPB},r_2], and r=[r_2,r_{BS}]. Here r_1=(r_{SPH} +r_{MPB})/2, r_2=(r_{MPB}+r_{BS})/2, r is the cylindrical radii from (0,0) in the Y-Z MSO plane and r_{MPB} and r_{BS} are the radial distances of the MPB and BS intersection at each plane, respectively. The value of the innermost boundary r_{SPH} corresponds to the cylindrical radii associated with the intersection between the plane under consideration and an effective spherical obstacle of radius 1.2 R_M. This methodology reduces the effects from crustal magnetic fields in the following calculations. If there is not such intersection, r_{SPH}=0R_M.

For each of these annular regions, we determine the centers of intensity $\langle\mathbf{r}\rangle_+$ and $\langle\mathbf{r}\rangle_-$ associated with all positions where Bx_{MSO}>0 and Bx_{MSO}<0, respectively. This calculation is analogous to the definition of the center of mass, but with the Bx_{MSO} component instead of the mass. Thus, this methodology makes use of the local magnetic field draping morphology, as implemented in Romanelli, Modolo, Leblanc, Chaufray, Hess, et al. (2018). Based on the two centers of intensity, we define a unitary vector (going from $\langle\mathbf{r}\rangle_+$ to $\langle\mathbf{r}\rangle_-$), used as a proxy to characterize the morphology of the magnetic field for each annular region in

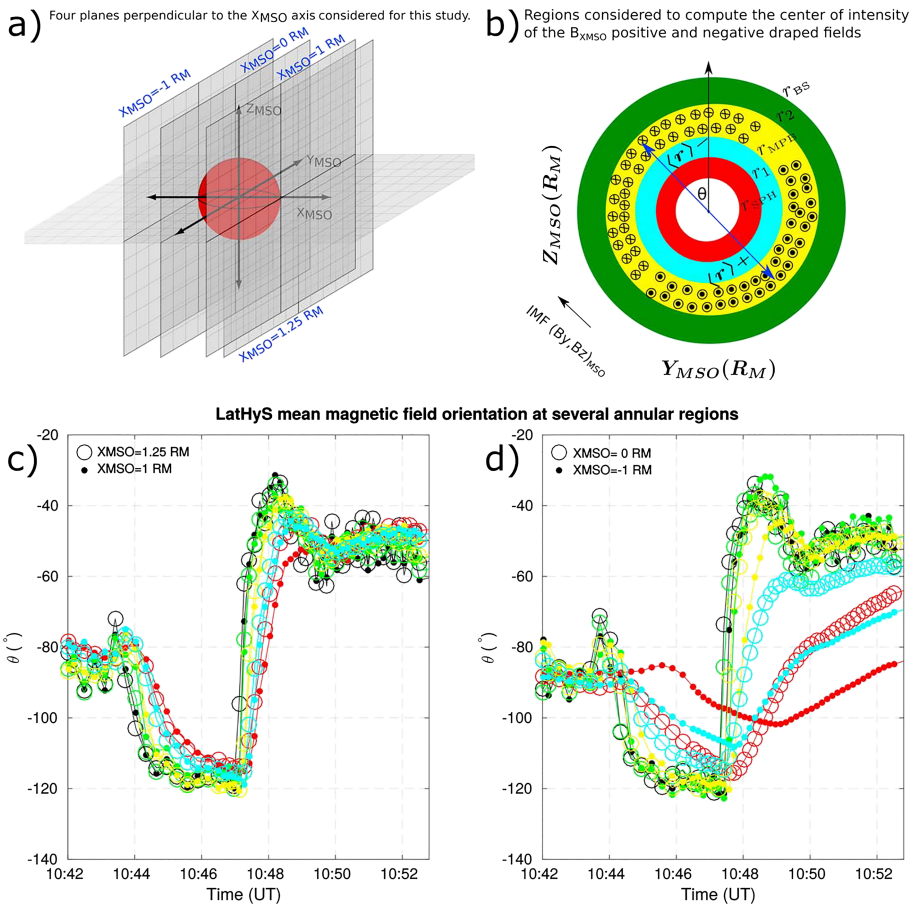

Figure 2. (a, b) Schematic representation of the four annular regions considered to study the magnetic field morphology in the specified four planes perpendicular to the X_{MSO} axis. (c, d) θ computed from the upstream interplanetary magnetic field component perpendicular to the X_{MSO} axis (in black) and the centers of magnetic field intensity in the four annular regions at the X_{MSO}=1.25R_M and X_{MSO}=1R_M planes (c), and at the X_{MSO}=0R_M, and X_{MSO}=−1R_M planes (d), as a function of time (for 23 December 2014, 10:42–10:52:30 UT). Green, yellow, light blue, and red curves characterize the mean magnetic field orientation over annular regions sampling from the magnetosheath up to the magnetic pileup region, for all analyzed planes. MSO = Mars Solar Orbital.

each of the four considered planes. By means of the associated angle θ, between such vector in the *Y*-*Z* MSO plane and the Z_{MSO} axis (varying between −180° and 180°), we study the temporal evolution of magnetic field morphology inside the dayside magnetic pileup region and magnetosheath (MSH), for the four planes and for the 10:42:00–10:52:48 UT time interval.

LatHyS results demonstrate that different sections of the dayside magnetosphere, in the four X_{MSO} slices described above (see Figure 2a), adapt to the IMF variability over several timescales (Figures 2c and 2d). This range in recovery timescales depends upon the physical properties and processes taking place in each dayside region. The simulation results are separated into two panels in Figures 2c and 2d for easy viewing with the colors referring to the annular regions (Figure 2b) where each sampling was performed. When comparing curves related to the same annular region (line colors), the results demonstrate a clear difference in the magnetic field recovery times between X_{MSO} planes. Indeed, for a given annular region, θ is generally observed to vary first in the X_{MSO} plane that is furthest upstream, as the magnetic perturbation propagates through the system. The temporal variability computed for the outer MSH magnetic field orientation (green curve) closely resembles the IMF rotation observed by MAVEN upstream from the Martian bow shock (black curve), after a short time delay on the order of ∼8 s or less. Next, the inner MSH region (yellow curve) also follows the IMF rotation, after a larger time delay that depends upon the X_{MSO} plane under consideration. The similarity between the perpendicular component of both the upstream IMF and the modeled MSH

suggests that the direction of the local magnetic field in the MSH is a reliable proxy for monitoring changes in the IMF clock angle, particularly upstream from the terminator plane.

A larger time shift and a smoother rotation of the local magnetic field is observed in the external and internal regions inside the MPB (light blue and red, respectively), as clearly seen in Figure 2d. This temporal evolution is due to the relatively smaller bulk velocity of the local plasma in this region, the energy exchange across the MPB, and the magnetic field diffusion into the Martian ionosphere.

The rate of change of θ with time (at a fixed X_{MSO} value), that is, the angular frequency (ω) associated with the rotation of the mean component of the local magnetic field perpendicular to the X_{MSO} axis, also varies with time as a function of the annular region and X_{MSO} plane. Table 1 displays the computed angular velocities for all annular regions at the X_{MSO}=1.25R_M and X_{MSO}=−1R_M planes. By analyzing the magnetic field morphology in these planes, we can clearly assess the differences and similarities in the Martian recovery timescales. As can be seen, relatively sharp and fast adaptations take place in the outer MSH, with ω up to ∼90% of the IMF angular velocity upstream from the bow shock at ∼10:44 and ∼10:47 UT (fastest IMF rotations during the time interval of interest, as shown in Figure 2). In contrast, smoother and slower rotations occur in the innermost regions. An additional difference is identified by comparing the resulting ratios between ω inside the MPB and that of the IMF rotation for both X_{MSO} planes. While this ratio varies between ∼47% and ∼56% for both IMF rotations at ∼10:44 and ∼10:47 UT (at X_{MSO}=1.25R_M), there are significant differences when computed at the X_{MSO}=−1R_M plane. Indeed, this ratio varies between 16% and 19% under the IMF rotation with ω=−31°/min, while such ratio varies between 5% and 11% for the IMF rotation with ω=106°/min. These angular ratios are found to generally decrease for increasing IMF rotation angular velocities, suggesting a limit for the expected angular velocities of each region downstream from the planet, when magnetic field diffusion is important. The ratios obtained for the X=−1R_M plane are similar to the ones computed for the Martian magnetotail, reported in Modolo et al. (2012) and Romanelli, Modolo, Leblanc, Chaufray, Hess, et al. (2018) and provide an order of magnitude to estimate the recovery timescales of different regions of the Martian magnetosphere associated with changes in the IMF clock angle. For instance, for the particular case of an ∼90° IMF rotation that lasts 50 s in the SW (last row in Table 1), we find that the recovery timescales of the Martian magnetosphere (up to the X_{MSO}=−1R_M plane) range between ∼8 s and ∼11 min, depending on the considered region. In particular, the slowest adaptation to the IMF variability takes place in the inner MPB region. The associated recovery timescale is computed as the sum of the time shift between the observed change in θ from ∼−120° to ∼−40° in the IMF (approximately at 10:47:25 UT, black curve in Figure 2d) and the observed response of the lobes in the inner MPB region (approximately at 10:48:58 UT, red curve in Figure 2d), and the necessary time for the lobes to reach equilibrium with the latter IMF configuration. In this particular case, the lobes require ∼10 min to evolve from θ∼−100° (orientation of the lobes approximately at 10:48:58 UT, red curve in Figure 2) to θ∼−50° with ω=5°/min. In this methodology we are implicitly assuming that each of the magnetospheric regions react to the two main IMF rotations during the time intervals specified in Table 1, after a time delay that is associated with the convection of the perturbation through the Martian magnetosphere.

3.2. O^+ Plume Recovery Timescales

The O^+ plume is made of planetary ions whose main acceleration mechanism involves the SW convective electric field. Under stationary conditions and for uniform magnetic and electric fields, the motion of such particles can be seen as the result of a drift velocity perpendicular to **B** and **E**, plus a gyromotion around **B**. Therefore, based on these conditions and, if spatial nonuniformities in the source of these particles are small, the vector $\mathbf{r}_{CM}$ defined from (0,0) to the center of mass of the O^+ plume computed in a *Y-Z* MSO plane must be parallel to the convective electric field at the same plane.

To estimate recovery timescales of the O^+ plume, we first estimate the center of mass of such ion population using the following criteria. We compute the mean O^+ density in a region bounded by two planes perpendicular to the X_{MSO} axis (separated by 400 km) and outside the nominal MPB (plus a 30% security window), between X_{MSO}=1R_M and X_{MSO}=−2.30R_M planes. The separation between planes is chosen to have a significant set of macroparticles (representing a cloud of ions with a given density and with the same charge, mass, velocity, and origin) to compute the center of mass, and as many center of mass estimations as possible to study the dynamics of the O^+ plume as a function of the X_{MSO} axis. We do not consider O^+ ions inside

Table 1
Estimations of the Angular Velocity for Different Regions Inside the Martian Magnetosphere for the $X_{MSO}=1.25R_M$ and $X_{MSO}=-1R_M$ Planes, as a Response to Two IMF Clock Angle Rotations During the Time Interval Under Study

Region (R_M)	$X_{MSO}=1.25R_M$				$X_{MSO}=-1R_M$			
	ω (°/min)	Time (UT)	N	Ratio	ω (°/min)	Time (UT)	N	Ratio
Inner MPB region	−16	10:43:44–10:45:53	8	47%	−5	10:45:35–10:48:58	20	16%
Outer MPB region	−17	10:43:44–10:45:53	8	50%	−6	10:44:39–10:47:43	15	19%
Inner MSH region	−21	10:43:44–10:45:35	7	62%	−18	10:44:02–10:46:12	8	58%
Outer MSH region	−30	10:43:25–10:44:40	5	88%	−27	10:44:02–10:45:34	6	87%
IMF	−34	10:43:25–10:44:40	5	—	−31	10:43:43–10:44:57	5	—
Inner MPB region	49	10:47:16–10:48:40	10	47%	5	10:48:58–10:52:31	23	5%
Outer MPB region	58	10:47:16–10:48:31	9	56%	12	10:47:43–10:49:53	15	11%
Inner MSH region	75	10:47:08–10:48:12	8	72%	49	10:47:35–10:49:07	11	46%
Outer MSH region	86	10:47:08–10:48:03	7	83%	91	10:47:25–10:48:21	7	86%
IMF	104	10:46:58–10:47:44	6	—	106	10:47:25–10:48:12	6	—

[a]From left to right, the columns display the region under analysis, the derived angular velocity, the time interval in which the angular velocity is computed, the number of points in such calculation, and the ratio between the computed angular velocity and that of the IMF rotation. MSO = Mars Solar Orbital; MPB = magnetic pileup boundary; MSH = magnetosheath; IMF = interplanetary magnetic field.

the MPB since they are mainly accelerated by other processes, for example, the ambipolar electric field and magnetic tension forces. Based on such mean density field, we compute the center of mass and associate its value to the X_{MSO} coordinate in between both planes. This procedure allows us to estimate the O^+ plume recovery timescales by studying the evolution of $\mathbf{r}_{CM}$, the mean convective electric field upstream from the bow shock in the same spatial region, and the angle between them, as a function of time and X_{MSO}. We study the O^+ plume recovery process up to $X_{MSO}=-2.30$ R_M so that, together with the results by Romanelli, Modolo, Leblanc, Chaufray, Hess, et al. (2018), we provide a description of the magnetosphere and O^+ plume recovery between $X_{MSO}=1R_M$ and $X_{MSO}=-2.30R_M$.

Figure 3a shows the clock angle associated with $\mathbf{r}_{CM}$ (blue curve) and the convective electric field (red curve) as a function of time, for two different X_{MSO} planes at $X_{MSO}=1R_M$ and $X_{MSO}=-2.30R_M$. The associated angular difference as a function time is shown in black. As can be seen, the angular difference is initially small at both planes. As soon as the IMF rotation reaches the planes under consideration, the convective electric field rotates but given that the O^+ plume is not able to adapt fast enough, the angular difference between **E** and the O^+ plume increases. Similar profiles as a function of time are found for all analyzed planes. We define two O^+ recovery timescales associated with each plane as follows. The first one is defined by the time interval during which the angular difference between **E** and the O^+ plume direction is larger than a chosen threshold, for instance, 10° (brown arrows). Therefore, this recovery timescale is the time the O^+ plume demands to follow up the electric field transition from a clock angle around 300° (State 1) to 230° (State 2). The second recovery timescale is twice the time interval between the beginning of the electric field rotation (angular difference larger than the chosen threshold) and the maximum clock angle difference (black arrows). The factor 2 is associated with the time interval required for the O^+ plume to be aligned with the new electric field direction, right after the maximum angular difference between both vectors has been reached. As can be seen, the O^+ recovery timescale in the plane downstream from the planet is larger than that in the dayside, regardless of the considered definition. It is worth pointing out that any estimated recovery timescale will be limited by the temporal resolution, which in this case is the time interval between analyzed simulated magnetospheric states (between simulation snapshots). The simulation temporal resolution (snapshot) during the analyzed time interval is 9.25 or 18.5 s. Thus, the estimated uncertainty in the estimated timescales is 9.25 s.

Figure 3b displays the sliding average of the computed O^+ plume recovery timescales (T_{REC}) over 4,000 km, as a function of the X_{MSO} coordinate. The bars are associated with the variability of the 4,000-km sliding average of T_{REC} for a clock angle difference threshold (dashed orange line in Figure 3a) varying between 5° and 15°. We chose to perform averages over 4,000 km (on the order of the planetary scale) to analyze the large-scale trend between T_{REC} and X_{MSO}, overcoming nonphysical jumps in the estimated recovery timescales that are only associated with the time interval between considered simulation snapshots. As

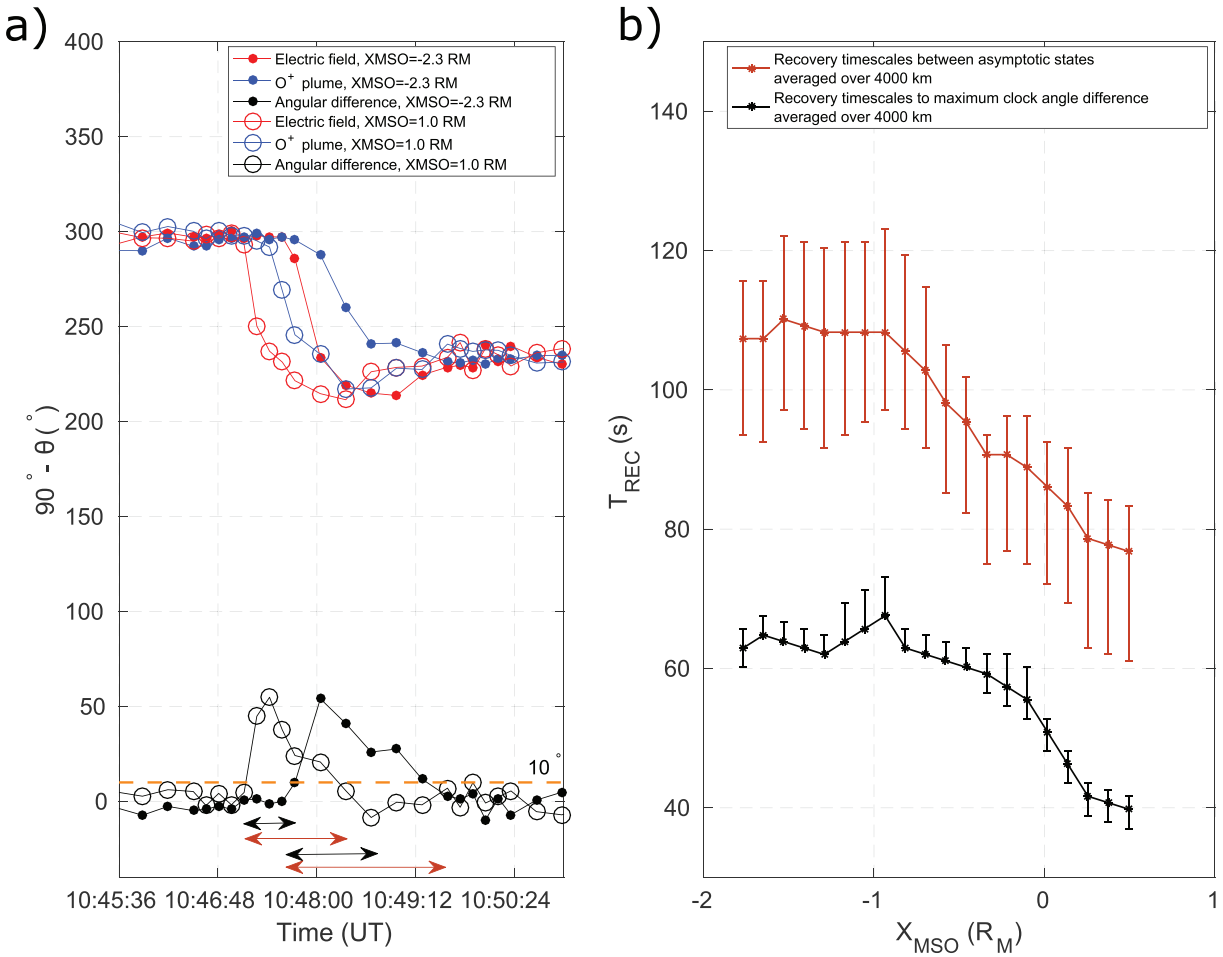

Figure 3. (a) Clock angle of the convective electric field (in red), the center of mass of the O^+ plume (in blue), and the angular shift between them (in black) for two planes perpendicular to the X_{MSO}, from LatHyS results. (b) Sliding average of the estimated recovery timescales of the O^+ plume to such changes in the convective electric field orientation, as a function of X_{MSO}.

can be seen, estimated O^+ averaged recovery timescales range between ~40 s (80 s) and ~60 s (110 s) based on the definition associated with the maximum clock angle difference (time interval between State 1 and State 2), for X_{MSO} ranging between 0.5 and −1.75 R_M.

4. Discussion and Conclusions

In this study we have analyzed a time-dependent LatHyS run that takes into account MAVEN magnetic field and plasma observations, in order to improve our understanding on the responses of the Martian magnetosphere to changes in the IMF orientation.

First, we find a time shift in the observed changes in the magnetic field morphology between the considered X_{MSO} planes (seen, e.g., in Figure 2c) associated with the transit time of the perturbation convected by the local plasma from one plane to another. In addition, the results presented in the previous section imply that the magnetotail will not rotate as fast as one might expect based only on changes in the external conditions and plasma velocities in the wake. That is, instead of a magnetotail rotation with θ covering the IMF clock angle range observed upstream from the bow shock, such rotation would be restricted to a significantly smaller clock angle range (seen, for instance, in the red curves in Figure 2d). Thus, these results suggest that there are serious limitations to estimate the IMF clock angle based on measurements in the Martian magnetotail, under nonstationary conditions. Such limitations are particularly important for events where IMF variability can be understood in terms of a set of rotations whose axes are not aligned. When the event under analysis is mainly a rotation along a fixed axis (with a fixed sense of rotation), the magnetotail θ range will be very

similar to that of the upstream IMF, given that a new magnetic field configuration consistent with such external condition must be achieved. Comparison between Figure 2 and Figure 9 of Romanelli, Modolo, Leblanc, Chaufray, Hess, et al. (2018) shows that differences in the adaptation of a given (fixed) annular region are drastically more important between the $X_{\mathrm{MSO}}=1R_M$ and $X_{\mathrm{MSO}}=-1R_M$ planes than outside from this region.

Second, we have determined ratios between the angular velocity associated with the recovery of the dayside magnetic field morphology in the MSH and magnetic pileup region and the associated IMF rotation observed by MAVEN upstream from the Martian bow shock. Such ratios provide recovery timescales of the dayside Martian magnetosphere normalized by the IMF clock angle variability. These estimations provide complementary information to studies interested in determining proxies for the IMF under quasi-stationary external conditions, based on the magnetic field morphology inside the Martian magnetosphere (Fang et al., 2018; Hurley et al., 2018).

Third, we also find that the associated recovery timescales of the O^+ plume range between 40 and 110 s and take greater values for further downstream distances (for both black and brown curves in Figure 3b), at least up to $X_{\mathrm{MSO}}=-1R_M$. The interpretation for such increase is the following. Since we compute the center of mass for particles outside the MPB, the local plasma velocity around it is on the order of the local MSH velocities. Given that the convective electric field upstream from the bow shock is convected with the SW velocity, the time interval needed for a region to adapt to the new **E** orientation must increase going further in the downstream direction. The observed trends in Figure 3b are not successfully fitted with straight lines, as a result of changes in the bulk plasma velocity in the MSH (e.g., acceleration in the flanks), nonuniformity of **E** inside the bow shock and differences in the distance traveled by particles sampled at a fixed plane but whose source is located at different positions. Despite these factors, it is interesting to compare the computed O^+ recovery timescales, with an estimation for the O^+ gyroperiod in the MSH, given that the center of mass of the O^+ is typically found in this magnetospheric region. A O^+ subject to a magnetic field with $|B|\sim 20$ nT has an associated gyroperiod of ~ 52 s. Thus, the computed O^+ recovery timescales are on the same order of the local O^+ gyrofrequency, confirming that the O^+ plume recovery is a kinetic process. Finally, since the O^+ ions will end up assimilated by the SW, an asymptotic recovery timescale could be expected. The observed scatter in T_{REC} in the explored X_{MSO} range (particularly in the brown curve) prevents from assessing whether such asymptote is present or reached at further downstream distances.

A future study on effects on the Martian magnetosphere from changes in the IMF and SW properties over different timescales should be considered to further explore the region of validity of the conclusions of this work.

Acknowledgments
The MAVEN mission is supported by NASA through the Mars Scout program. N. R. is supported by a Postdoctoral Research Associate appointment at NASA Goddard Space Flight Center, administrated by Center for Research and Exploration in Space Sciences and Technology II and University of Maryland, Baltimore County (UMBC). N. R. would like to thank J. Connerney for useful comments and suggestions. N. R., R. M., and F. L. are indebted to ANR for the project TEMPETE (ANR-17-CE31-0016). N. R. is also indebted to the French Space Agency CNES for its support. Authors also acknowledge the support of the IPSL data center CICLAD for providing us access to their computing resources. MAVEN data are publicly available through the Planetary Data System (https://pds-ppi.igpp.ucla.edu/index.jsp). Numerical simulations outputs used in this article can be found online (http://impex.latmos.ipsl.fr.).

References

Acuña, M. H., Connerney, J. E. P., Ness, N. F., Lin, R. P., Mitchell, D., Carlson, C. W., et al. (1999). Global distribution of crustal magnetization discovered by the Mars Global Surveyor MAG/ER Experiment. *Science*, *284*, 790–793. https://doi.org/10.1126/science.284.5415.790

Acuña, M. H., Connerney, J. E. P., Wasilewski, P., Lin, R. P., Anderson, K. A., Carlson, C. W., et al. (1998). Magnetic field and plasma observations at Mars: Initial results of the Mars Global Surveyor mission. *Science*, *279*(5357), 1676–1680.

Brain, D. A., Barabash, S., Bougher, S., Duru, F., Jakosky, B., & Modolo, R. (2017). Solar wind interaction and atmospheric escape . In B. Haberle (Ed.), *in The Atmosphere and Climate of Mars* (pp. 464–496). Cambridge: Cambridge University Press. https://doi.org/10.1017/9781139060172

Cain, J. C., Ferguson, B. B., & Mozzoni, D. (2003). An $n=90$ internal potential function of the Martian crustal magnetic field. *Journal of Geophysical Research*, *108*(E2), 5008. https://doi.org/10.1029/2000JE001487

Connerney, J. E. P., Acuña, M. H., Ness, N. F., Kletetschka, G., Mitchell, D., Lin, R. P., & Reme, H. (2005). Tectonic implications of Mars crustal magnetism. *Proceedings of the National Academy of Sciences of the United States of America*, *102*(42), 14,970–14,975. https://doi.org/10.1073/pnas.0507469102

Connerney, J. E. P., Acuña, M. H., Wasilewski, P. J., Kletetschka, G., Ness, N. F., Réme, H., et al. (2001). The global magnetic field of Mars and implications for crustal evolution. *Geophysical Research Letters*, *28*, 4015–4018. https://doi.org/10.1029/2001GL013619

Connerney, J. E. P., Espley, J. R., DiBraccio, G. A., Gruesbeck, J. R., Oliversen, R. J., Mitchell, D. L., et al. (2015). First results of the MAVEN magnetic field investigation. *Geophysical Research Letters*, *42*, 8819–8827. https://doi.org/10.1002/2015GL065366

Connerney, J. E. P., Espley, J. R., Lawton, P., Murphy, S., Odom, J., Oliversen, R., & Sheppard, D. (2015). The MAVEN magnetic field investigation. *Space Science Review*, *195*, 257–291. https://doi.org/10.1007/s11214-015-0169-4

Curry, S. M., Luhmann, J. G., Ma, Y. J., Dong, C. F., Brain, D., Leblanc, F., et al. (2015). Response of Mars O^+ pick-up ions to the March 8th, 2015 ICME: Inferences from MAVEN data-based models. *Geophysical Research Letter*, *42*, 9095–9102. https://doi.org/10.1002/2015GL065304

DiBraccio, G. A., Dann, J., Espley, J. R., Gruesbeck, J. R., Soobiah, Y., Connerney, J. E. P., et al. (2017). MAVEN observations of tail current sheet flapping at Mars. *Journal of Geophysical Research: Space Physics*, *122*, 4308–4324. https://doi.org/10.1002/2016JA023488

DiBraccio, G. A., Espley, J. R., Gruesbeck, J. R., Connerney, J. E. P., Brain, D. A., Halekas, J. S., et al. (2015). Magnetotail dynamics at Mars: Initial MAVEN observations. *Geophysical Research Letter*, *42*, 8828–8837. https://doi.org/10.1002/2015GL065248

DiBraccio, G. A., Luhmann, J. G., Curry, S. M., Espley, J. R., Xu, S., Mitchell, D. L., et al. (2018). The twisted configuration of the Martian magnetotail: MAVEN observations. *Geophysical Research Letters*, *45*, 4559–4568. https://doi.org/10.1029/2018GL077251

Dong, Y., Fang, X., Brain, D. A., McFadden, J. P., Halekas, J. S., Connerney, J. E., et al. (2015). Strong plume fluxes at Mars observed by MAVEN: An important planetary ion escape channel. *Geophysical Research Letter*, *42*, 8942–8950. https://doi.org/10.1002/2015GL065346

Dubinin, E., & Fraenz, M. (2015). Magnetotails of Mars and Venus. In A. Keiling, C. M. Jackman, & P. Delamere (Eds.), *in Magnetotails in the solar system* (Vol. 207, pp. 43–59), *Geophysical Monograph Series*. Washington, DC: American Geophysical Union. https://doi.org/10.1002/9781118842324.ch3

Dubinin, E., Fraenz, M., Fedorov, A., Lundin, R., Edberg, N., Duru, F., & Vaisberg, O. (2011). Ion energization and escape on Mars and Venus. *Space Science Review*, *162*, 173–211.

Fang, X., Ma, Y., Luhmann, J. G., Dong, Y., Brain, D. A., Hurley, D. M., et al. (2018). The morphology of the solar wind magnetic field draping on the dayside of Mars and its variability. *Geophysical Research Letters*, *45*, 3356–3365. https://doi.org/10.1002/2018GL077230

Grigorenko, E. E., Shuvalov, S. D., Malova, H. V., Dubinin, E., Popov, V. Y., Zelenyi, L., et al. (2017). Imprints of quasi-adiabatic ion dynamics on the current sheet structures observed in the Martian magnetotail by MAVEN. *Journal of Geophysical Research: Space Physics*, *122*, 10,176–10,193. https://doi.org/10.1002/2017JA024216

Halekas, J. S., Brain, D. A., Luhmann, J. G., DiBraccio, G. A., Ruhunusiri, S., Harada, Y., & Jakosky, B. M. (2017). Flows, fields, and forces in the Mars-solar wind interaction. *Journal of Geophysical Research: Space Physics*, *2*, 11,320–11,341. https://doi.org/10.1002/2017JA024772

Halekas, J. S., Ruhunusiri, S., Harada, Y., Collinson, G., Mitchell, D. L., Mazelle, C., et al. (2017). Structure, dynamics, and seasonal variability of the Mars-solar wind interaction: MAVEN solar wind ion analyzer in-flight performance and science results. *Journal of Geophysical Research: Space Physics*, *122*, 547–578. https://doi.org/10.1002/2016JA023167

Halekas, J. S., Taylor, E. R., Dalton, G., Johnson, G., Curtis, D. W., McFadden, J. P., et al. (2015). *The solar wind ion analyzer for MAVEN* (Vol. *195*, pp. 125–151). https://doi.org/10.1007/s11214-013-0029-z

Harada, Y., Halekas, J. S., McFadden, J. P., Mitchell, D. L., Mazelle, C., Connerney, J. E. P., et al. (2015a). Magnetic reconnection in the near-Mars magnetotail: MAVEN observations. *Geophysical Research Letters*, *42*, 8838–8845. https://doi.org/10.1002/2015GL065004

Harada, Y., Halekas, J. S., McFadden, J. P., Mitchell, D. L., Mazelle, C., Connerney, J. E. P., et al. (2015b). Marsward and tailward ions in the near-Mars magnetotail: MAVEN observations. *Geophysical Research Letter*, *42*, 8925–8932. https://doi.org/10.1002/2015GL065005

Hurley, D. M., Dong, Y., Fang, X., & Brain, D. A. (2018). A proxy for the upstream IMF clock angle using MAVEN magnetic field data. *Journal of Geophysical Research: Space Physics*, *123*, 9612–9618. https://doi.org/10.1029/2018JA025578

Jakosky, B. M., Brain, D., Chaffin, M., Curry, S., Deighan, J., Grebowsky, J., et al. (2018). Loss of the Martian atmosphere to space: Present-day loss rates determined from MAVEN observations and integrated loss through time. *Icarus*, *315*, 146–157. https://doi.org/10.1016/j.icarus.2018.05.030

Jakosky, B. M., Lin, R. P., Grebowsky, J. M., LuhmannD, J. G., Mitchell, F., Beutelschies, G., et al. (2015). The Mars Atmosphere and Volatile EvolutioN (MAVEN) mission. *Space journal Review*, *195*(1-4), 3–48. https://doi.org/10.1007/s11214-015-0139-x

Leclercq, L., Modolo, R., Leblanc, F., Hess, S., & Mancini, M. (2016). 3D magnetospheric parallel hybrid multi-grid method applied to planet-plasma interactions. *Journal of Computational Physics*, *309*, 295–313. https://doi.org/10.1016/j.jcp.2016.01.005

Luhmann, J. G., Dong, C., Ma, Y., Curry, S. M., Mitchell, D. L., Espley, J. R., et al. (2015). Implications of MAVEN Mars near-wake measurements and models. *Geophysical Research Letter*, 42. https://doi.org/10.1002/2015GL066122

Ma, Y. J., et al. (2017). Variations of the Martian plasma environment during the ICME passage on 8 March 2015: A time-dependent MHD study. *Journal of Geophysical Research: Space Physics*, *122*, 1714–1730. https://doi.org/10.1002/2016JA023402

Martinez, A., Leblanc, F., Chaufray, J. Y., Modolo, R., Romanelli, N., Curry, S., et al. (2019). Variability of precipitating ion fluxes during the September 2017 event at Mars. *Journal of Geophysical Research: Space Physics*, *124*, 420–432. https://doi.org/10.1029/2018JA026123

Mazelle, C., Winterhalter, D., Sauer, K., Trotignon, J. G., Acuña, M. H., Baumgärtel, K., et al. (2004). Bow shock and upstream phenomena at Mars. *Space Science Review*, *111*, 115–181.

McFadden, J., et al. (2015). The MAVEN SupraThermal And Thermal Ion Compostion(STATIC) instrument. *Space Science Review*, *195*, 199–256. https://doi.org/10.1007/s11214-015-0175-6

Modolo, R., Chanteur, G. M., & Dubinin, E. (2012). Dynamic Martian magnetosphere: Transient twist induced by a rotation of the IMF. *Geophysical Research Letter*, *39*, L01106. https://doi.org/10.1029/2011GL049895

Modolo, R., Chanteur, G. M., Dubinin, E., & Matthews, A. P. (2005). Influence of the solar EUV flux on the Martian plasma environment. *Annales Geophysicae*, *23*, 433–444. https://doi.org/10.5194/angeo-23-433-2005

Modolo, R. (2016). Mars-solar wind interaction: LatHyS, an improved parallel 3-D multispecies hybrid model. *Journal of Geophysical Research: Space Physics*, *121*, 6378–6399. https://doi.org/10.1002/2015JA022324

Modolo, R., Hessb, S., Génot, V., Leclercq, L., Leblanc, F., Chaufray, J.-Y., et al. (2017). *The LatHyS database for planetary plasma environment investigations* (Vol. *13*, pp. 13–21). Overview and a case study of data/model comparisons: Planetary and Space Science. https://doi.org/10.1016/j.pss.2017.02.015

Rahmati, A., Rahmati, A., Larson, D. E., Cravens, T. E., Lillis, R. J., Halekas, J. S., et al. (2017). MAVEN measured oxygen and hydrogen pickup ions: Probing the Martian exosphere and neutral escape. *Journal of Geophysical Research: Space Physicss*, *122*, 3689–3706. https://doi.org/10.1002/2016JA023371

Richer, E., Modolo, R., Chanteur, G. M., Hess, S., & Leblanc, F. (2012). A global hybrid model for Mercury's interaction with the solar wind: Case study of the dipole representation. *Journal of Geophysical Research*, *117*, A10228. https://doi.org/10.1029/2012JA017898

Romanelli, N., Bertucci, C., Gómez, D., & Mazelle, C. (2015). Dependence of the location of the Martian magnetic lobes on the interplanetary magnetic field direction: Observations from Mars Global Surveyor. *Journal of Geophysical Research: Space Physics*, *120*, 7737–7747. https://doi.org/10.1002/2015JA021359

Romanelli, N., Gómez, D., Bertucci, C., & Delva, M. (2014). Steady-state magnetohydrodynamic flow around an unmagnetized conducting sphere. *The Astrophysical Journal*, *789*(1), 43.

Romanelli, N., Modolo, R., Leblanc, F., Chaufray, J.-Y., Hess, S., Brain, D., et al. (2018). Effects of the crustal magnetic fields and changes in the IMF orientation on the magnetosphere of Mars: MAVEN observations and LatHyS result. *Journal of Geophysical Research:Space Physics*, *123*, 5315–5333. https://doi.org/10.1029/2017JA025155

Romanelli, N., Modolo, R., Leblanc, F., Chaufray, J.-Y., Martinez, A., Ma, Y., et al.(2018). Responses of the Martian magnetosphere to an interplanetary coronal mass ejection: MAVEN observations and LatHyS results. *Geophysical Research Letters*, *45*, 7891–7900. https://doi.org/10.1029/2018GL077714

Sánchez-Cano, B., Sánchez-Cano, Hall, B. E. S, Lester, M., Mays, M. L., Witasse, O., et al. (2017). Mars plasma system response to solar wind disturbances during solar minimum. *Journal of Geophysical Research: Space Physics*, *122*, 6611–6634. https://doi.org/10.1002/2016JA023587

Turc, L., Fontaine, D., Savoini, P., & Modolo, R. (2015). 3D hybrid simulations of the interaction of a magnetic cloud with a bow shock. *Journal of Geophysical Research: Space Physics*, *120*, 6133–6151. https://doi.org/10.1002/2015JA21318

Vignes, D., Mazelle, C., Rme, H., Acuña, M. H., Connerney, J. E. P., Lin, R. P., et al. (2000). The solar wind interaction with Mars: Locations and shapes of the bow shock and the magnetic pile-up boundary from the observations of the MAG/ER experiment onboard MGS. *Geophysical Research Letters*, *27*(1), 49–52.